Energy Shaping Control for Robotic Needle Insertion

Enrico Franco
Mechanical Engineering Department
Imperial College London
London, UK
ef1311@imperial.ac.uk

Timothy Brown
Mechanical Engineering Department
Imperial College London
London, UK
timothy.brown15@imperial.ac.uk

***Abstract*—This work investigates the use of energy shaping control to reduce deflection in slender beams with tip load and actuation at the base. The ultimate goal of this research is a buckling avoidance strategy for robotic-assisted needle insertion. To this end, the rigid-link model of a flexible beam actuated at the base and subject to tip load is proposed, and an energy shaping approach is employed to construct a nonlinear controller that accounts for external forces. A comparative simulation study highlights the benefits of the proposed approach over a linear control baseline and a simplified nonlinear control.**

Keywords— Nonlinear Control, Underactuated Robots, Flexible Robots

I. Introduction

Needle deflection represents one of the main causes of error in traditional percutaneous interventions and can require repeated insertions, causing patient discomfort and increased duration of the clinical procedure [1], [2]. Robot-assisted needle insertion has the potential to improve accuracy and safety in percutaneous intervention and diagnosis. Typically, providing this functionality requires the ability to measure or estimate the insertion force and the needle deflection [3], [4], the provision of haptic feedback to the clinician, and a force or position control algorithm with proved stability and robustness to disturbances [5], [6]. Needle deflection can occur at any point during the insertion, depending on the needle geometry and on the forces acting on it. Insertion forces depend on insertion speed, insertion depth, tissue characteristics, and typically peak during or immediately after the puncture phase [7]. A comprehensive review of the strategies devised to control needle deflection can be found in [8]. Notable solutions include: the controlled rotation of bevel-tip needles [9]; a programmable needle tip consisting of multiple segments actuated independently [10]; steerable needles actuated by heat which is transmitted employing an optic fiber [11].

Slender needles, such as those used in biopsy, are particularly prone to buckling, which manifests itself as sudden lateral deflection when the axial force reaches the buckling load. While the risk of buckling can be mitigated employing stiffer needles with larger diameter, this approach is not desirable for biopsies due to increased patient discomfort. Taking inspiration from nature, a number of design principles that can reduce the risk of buckling have been highlighted in [12], however their implementation is often limited by manufacturing capabilities. In parallel, increasing attention has been drawn to the study of force control strategies for buckling avoidance [13]. Among the most notable approaches, a model predictive control for bevel-tip needles was presented in [14]. The application of a lateral force to the needle near the insertion point was proposed in [15], while an optimized path planning procedure for insertions in multi layered tissues was presented in [16]. Notable results in modelling and control of slender beams with tip load, which are representative of needle insertion, include: an integral LQR control for buckling avoidance of columns with piezoelectric actuators at both ends [17]; Hamiltonian models of a beam actuated at the base employing modal decomposition approaches in [18]; energy shaping control of a flexible beam with tip load in [19]–[21]. In practice however, actuators can often be placed only at the needle base, while linear controllers are only intended for small deflection. In summary, controlling needle insertion in the presence of lateral deflections remains an open problem.

In this work an energy shaping control approach is employed to reduce lateral deflection in slender beams with tip load and actuation at the base. Energy shaping control is ideally suited for underactuated systems, can be combined with adaptive algorithms [22]–[24], and has been applied successfully to several mechanical systems [25]. For controller design purposes, an underactuated rigid-link model of the slender beam is constructed employing the pseudo-rigid-body paradigm [26], which is then related to the Euler-Bernoulli (EB) theory. A nonlinear controller is designed employing a port-controlled Hamiltonian formulation and stability conditions are discussed. Finally, the effectiveness of the proposed controller is demonstrated with simulations employing a representative model of the insertion forces.

The rest of the paper is organized as follows: in Section II the system model is detailed and the energy shaping control formulation is briefly summarized. The controller design is outlined in Section III, while the simulation results are presented in Section IV. Concluding remarks and suggestions for future work are summarized in Section V.

II. Problem Formulation

A. System Model

Considering that insertion forces typically peak during the initial puncture and that the free length of the needle is then at the maximum, lateral deflection is particularly likely to occur in this condition, which is taken as reference in this work. Lateral forces acting on the needle due to the surrounding tissue are typically small in this case and are neglected for simplicity, while buckling and deflection generally occur according to the first mode shape. The needle is represented as a cantilever beam of length L with axial load F_y applied at the tip and is approximated with a planar rigid-link model mounted on an actuated base (Figure 1). The model parameters are the length l of the link and the elastic constant k_t, which are defined as in [26], where E is the Young's modulus and I is the area moment of inertia of the beam.

$$l = \gamma_\theta L$$
$$k_t = \gamma_\theta k_\theta EI/L \tag{1}$$

The parameters γ_θ, k_θ depend on the boundary conditions and on the load type, as defined in [27]. The resulting rigid-link system has two degrees-of-freedom (DOF): the translation of the base q_1, and the rotation of the link q_2.

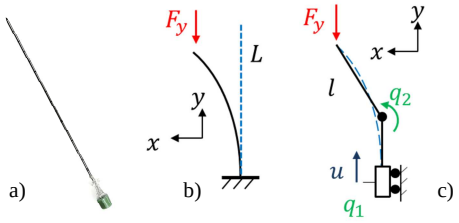

Fig. 1. a) Coaxial needle for percutaneous interventions; b) schematic of cantilever beam with first mode shape; c) corresponding rigid-link model.

Since only the translation of the base is actuated, the system has underactuation degree one. The equations of motion on the coordinate axes y, x are:

$$\begin{cases} (M+m)\ddot{q}_1 - ml\sin(q_2)\,\ddot{q}_2 - ml\cos(q_2)\,\dot{q}_2^2 = u - F_y \\ -ml\sin(q_2)\,\ddot{q}_1 + ml^2\ddot{q}_2 = -k_t\,q_2 + F_y l\sin(q_2) \end{cases} \tag{2}$$

The mass M refers to the actuated base, while m is the mass of the unactuated link. The set of attainable equilibria q_2^* is defined setting $\dot{q} = \ddot{q} = 0$ in (2). Assuming $q_2^* \cong 0$ and replacing $\sin(q_2^*)$ with a truncated Taylor series gives:

$$q_2^* = 0 \tag{3.a}$$
$$q_2^* = \pm\sqrt{6\left(1 - k_t/F_y l\right)} \tag{3.b}$$

The equilibrium (3.a) corresponds to the straight beam, while (3.b) exist only if $F_y > k_t/l$ and represent the buckled configurations. Substituting (1) in the above inequality gives:

$$F_y > k_\theta EI/L^2, \tag{4}$$

where $k_\theta \cong 2.4$ for this loading condition [27]. Thus (4) corresponds with good approximation to the first EB buckling load (i.e. $P_1 = (\pi/2)^2 EI/L^2$). In summary, the rigid-link system (2) is a good approximation of continuous EB models and is suitable for control purposes, as indicated in [20], [28] and included references.

B. *Overview of Energy Shaping Control*

The open-loop dynamics of a generic n DOF underactuated system without physical damping can be expressed in Hamiltonian form as follows:

$$\begin{bmatrix}\dot{q}\\ \dot{p}\end{bmatrix} = \begin{bmatrix}0 & I\\ -I & 0\end{bmatrix}\begin{bmatrix}\nabla_q H\\ \nabla_p H\end{bmatrix} + \begin{bmatrix}0\\ G\end{bmatrix}u \tag{5}$$

The position $q \in \mathbb{R}^n$ and the momenta $p = \mathcal{M}\dot{q} \in \mathbb{R}^n$ represent the system states. The control input $u \in \mathbb{R}^m$ affects the system dynamics through the mapping $G(q) \in \mathbb{R}^{n\times m}$, with $\mathrm{rank}(G) = m < n$. The open-loop Hamiltonian is defined as $H = T(q,p) + V(q)$, where $T(q,p) = \frac{1}{2}p^T\mathcal{M}^{-1}p$ is the kinetic energy, $\mathcal{M}(q) = \mathcal{M}^T > 0$ is the inertia matrix, and $V(q)$ is the open-loop potential energy. The $n \times n$ identity matrix is indicated with I, the symbol $\nabla_q(\cdot)$ represents the gradient in q, while $\nabla_p(\cdot)$ is the gradient in p.

The control aim for underactuated systems corresponds to stabilizing the attainable equilibrium $(q,p) = (q^*, 0)$, which is generally unstable in open-loop. Among the different energy shaping control formulations, Interconnection-and-Damping-Assignment Passivity-Based-Control (IDA-PBC) is employed here to achieve the following closed-loop dynamics [22]:

$$\begin{bmatrix}\dot{q}\\ \dot{p}\end{bmatrix} = \begin{bmatrix}0 & \mathcal{M}^{-1}\mathcal{M}_d\\ -\mathcal{M}_d\mathcal{M}^{-1} & J_2 - Gk_vG^T\end{bmatrix}\begin{bmatrix}\nabla_q H_d\\ \nabla_p H_d\end{bmatrix} \tag{6}$$

The closed-loop Hamiltonian is $H_d = \frac{1}{2}p^T\mathcal{M}_d^{-1}p + V_d$, the closed-loop inertia matrix is $\mathcal{M}_d$, while $J_2 = -J_2^T$ is a free matrix, and $k_v = k_v^T > 0$ is a tuning parameter. As a result of IDA-PBC, the desired equilibrium becomes a strict minimizer of the closed-loop potential energy V_d, thus $\nabla_q V_d(q^*) = 0$ and $\nabla_q^2 V_d(q^*) > 0$. Equating (5) and (6) and defining the pseudo inverse of G as $G^\dagger = (G^TG)^{-1}G^T$ in case of underactuation, the IDA-PBC control law becomes:

$$u = u_{es} + u_{di}$$
$$u_{es} = G^\dagger\left(\nabla_q H - \mathcal{M}_d\mathcal{M}^{-1}\nabla_q H_d + J_2\mathcal{M}_d^{-1}p\right) \tag{7}$$
$$u_{di} = -k_v G^T\nabla_p H_d$$

The energy shaping control u_{es} assigns the equilibrium q^*, while the damping-assignment u_{di} ensures asymptotic stability of $(q,p) = (q^*, 0)$. The design parameters (i.e. the matrix $\mathcal{M}_d$, J_2, and the potential energy V_d) should satisfy the following set of partial-differential-equations (PDE) $\forall (q,p) \in \mathbb{R}^{2n}$, which are termed kinetic-energy PDE and potential-energy PDE:

$$G^\perp\left(\nabla_q(p^T\mathcal{M}^{-1}p) - \mathcal{M}_d\mathcal{M}^{-1}\nabla_q(p^T\mathcal{M}_d^{-1}p)\right) + G^\perp(2J_2\mathcal{M}_d^{-1}p) = 0 \tag{8.a}$$
$$G^\perp\left(\nabla_q V - \mathcal{M}_d\mathcal{M}^{-1}(\nabla_q V_d)\right) = 0 \tag{8.b}$$

The term $G^\perp$ is a full-rank left annihilator of G and is defined so that $G^\perp G = 0$. Notably, setting $\mathcal{M}_d = k_m\mathcal{M}$ and $J_2 = 0$ verifies (8.a), while (8.b) becomes:

$$G^\perp\left(\nabla_q V - k_m\nabla_q V_d\right) = 0 \tag{9}$$

This particular choice serves as starting point for the controller design in the following section.

III. Controller Design

The proposed control relies on the following assumptions.

Assumption 1: The model parameters are exactly known.

Assumption 2: The position $q = (q_1, q_2)$ and the velocity $\dot{q}$ are measurable. Additionally, $|q_1| < l \ll 1$ and $|q_2| < \pi/2$.

Assumption 3: The force $F_y \geq 0$ is measurable, bounded, and slowly varying.

Notably *Assumption 1* is verified if the needle geometry is known. *Assumption 2, 3* are verified for system (2) since the force F_y and the position of the actuated base q_1 can be directly measured with sensors, while the angle q_2 is uniquely

identified by the deflection of the tip, which can be measured with a sensor or can be estimated with an observer [3]. The needle tip points towards the tissue (i.e. $|q_2| < \pi/2$), and the insertion depth is limited by the needle length (i.e. $|q_1| < l$ and typically $0.05 < l < 0.2$, thus $l \ll 1$ m) Finally the insertion force typically varies in the range $0 \leq F_y \leq 10$ N.

A. Partial Feedback Linearization

The first step in the proposed design procedure consists in applying a partial feedback linearization to (2) to obtain an equivalent system with constant inertia matrix $\mathcal{M}' = I$. Pre-multiplying both sides of (2) by $\mathcal{M}^{-1}$ we obtain:

$$\begin{cases} \ddot{q}_1 = v - F_y \dfrac{\cos(q_2)^2}{M + m\cos(q_2)^2} \\ \ddot{q}_2 = \dfrac{\sin(q_2)}{l} v - \dfrac{k_t}{ml^2} q_2 + F_y \dfrac{M \sin(q_2)}{m^2 l \cos(q_2)^2 + Mml} \end{cases} \tag{10}$$

The term v is the new control input and is related to u according to the following equation:

$$u = (M + m\cos(q_2)^2)v + \frac{q_2 \sin(q_2)\, k_t}{l} - ml\cos(q_2)\dot{q}_2^2 \tag{11}$$

The energy shaping control v is subsequently designed based on the open-loop dynamics (10) and results in a nonlinear control law (see *Remark 1*).

B. Energy Shaping Control

Differently from the canonical system (5), the open-loop dynamics (10) contains the external force F_y. Consequently, a modified energy shaping control is defined, where W is the work of the external forces:

$$u'_{es} = G^{\dagger}\left(\nabla_q H - \nabla_q W - k_m \nabla_q H'_d\right) \tag{12}$$

The new Hamiltonian H'_d in (12) accounts for the work W according to the potential-energy PDE, which becomes:

$$G^{\perp}\left(\nabla_q V - \nabla_q W - k_m \nabla_q V'_d\right) = 0 \tag{13}$$

For system (2), $V = k_t q_2^2/2$ and $W = -F_y(q_1 + l\cos(q_2))$. As a consequence of partial feedback linearization, the input matrix for system (10) is $G' = [1 \quad \sin(q_2)/l]^T$ and its left annihilator is $G'^{\perp} = [-\sin(q_2)/l \quad 1]$, which substituted in (13) gives:

$$-\frac{\partial V'_d}{\partial q_1}\frac{1}{l}\sin(q_2) + \frac{\partial V'_d}{\partial q_2} = \frac{k_t\, q_2}{ml^2 k_m} - F_y \frac{\sin(q_2)}{mlk_m} \tag{14}$$

The PDE (14) admits the following set of solutions:

$$V'_d = F_y \frac{\cos(q_2)}{mlk_m} + \frac{k_t}{2ml^2 k_m} q_2^2 + \frac{k_p}{2k_m}\Phi(w) + \mathcal{C}, \tag{15}$$

where $w = q_1 - q_1^* - \frac{1}{l}\cos(q_2)$, and F_y is a numeric value known at any instant and bounded (see *Assumption 3*). The parameter $k_p > 0$ and the term $\Phi(\cdot)$ are chosen to satisfy the minimizer conditions $\nabla_q V'_d(q_1^*, q_2^*) = 0$ and $\nabla_q^2 V'_d(q_1^*, q_2^*) > 0$. The constant $\mathcal{C} > 0$ ensures positive definitiveness of V'_d. Defining $\Phi(w) = (\log(-wl))^2$ with q_1^* the prescribed position of the base (i.e. desired insertion depth) and $q_2^* = 0$ gives:

$$\nabla_q V'_d(q_1^*, q_2^*) = 0 \tag{16.a}$$
$$\nabla_q^2 V'_d(q_1^*, q_2^*) = k_p\left(k_t - F_y l\right)/(mk_m^2) \tag{16.b}$$

Notably, $\nabla_q^2 V'_d(q_1^*, q_2^*) > 0$ is satisfied only if $F_y < k_t/l$, which corresponds to the buckling load. It follows from (16) that buckling cannot be avoided for forces larger than the critical load P_1, which is reasonable if the beam is only actuated at the base. Finally, the general expression of the control law is:

$$v = G'^{\dagger}\left(\nabla_q V - \nabla_q W - k_m \nabla_q V'_d\right) - k_v G'^T \dot{q}/k_m \tag{17}$$

The stability conditions for the equilibrium $q = (q_1^*, 0)$ of the closed-loop system (10),(17) are discussed in the following result.

Proposition 1: Consider system (10) under *Assumption 1-3* in closed loop with control (17), where $k_p > 0, k_v > 0$, and $F_y < k_t/l$. Then $q^* = (q_1^*, 0)$ is a minimizer of V'_d and a locally asymptotically stable equilibrium of the closed-loop system.

Proof: It follows directly from (16) that q^* is a strict minimizer of $V_d{}'$ if $k_p > 0$ for any $F_y < k_t/l$.

To prove the stability claim, we introduce the work of the external forces in the open-loop dynamics (5):

$$\dot{p} = -\nabla_q H + \nabla_q W + G' u \tag{18}$$

Substituting (17) into (18) with $\mathcal{M}_d = k_m \mathcal{M}$ and $J_2 = 0$ recovers (6), with $H'_d = \frac{1}{2} p^T \mathcal{M}_d^{-1} p + V'_d$. Observing that $V'_d > 0$ under *Assumption 1-3*, we take the Lyapunov function candidate $H'_d = \frac{1}{2} p^T \mathcal{M}_d^{-1} p + V'_d$, which is positive definite and radially unbounded. Computing the time derivative of H'_d while substituting (6) gives:

$$\begin{aligned} \dot{H}'_d &= \nabla_q H_d'^T \dot{q} + \nabla_p H_d'^T \dot{p} + \dot{V}'_d \\ &= -\nabla_p H_d'^T G' k_v G'^T \nabla_p H'_d + \dot{V}'_d \\ &= -k_v \left(\frac{z}{k_m}\right)^2 + \dot{F}_y \frac{\cos(q_2)}{mlk_m} \leq 0 \end{aligned} \tag{19}$$

At equilibrium $\dot{F}_y = 0$ thus it follows from (19) that $z = G'^T \dot{q}$ converges to zero and q^* is a stable equilibrium. To verify asymptotic stability, we study the trajectories of (10)-(17) restricted to the manifold $z(t) = 0\ \forall t$, recalling that $\mathcal{M}' = I$ hence $p = \dot{q}$ and $\dot{p} = \ddot{q}$:

$$z = \dot{q}_1 + (\dot{q}_2 \sin(q_2)) / l = 0 \tag{20}$$

$$\begin{aligned} \dot{z} = \frac{\sin(q_2)}{lk_m}\left(\frac{k_t q_2}{l^2 m} - \left(\frac{F_y}{lm} + \frac{k_p \log(w)}{w}\right)\sin(q_2)\right) \\ + \dot{q}_2^2 \cos(q_2)/l - \frac{k_p \log(w)}{wk_m} = 0 \end{aligned} \tag{21}$$

Imposing $\ddot{z} = 0$ and substituting (20),(21) provides two solutions: $\dot{q}_2 = 0$ and $q_2 = 0$. From (20) we conclude that in either case $\dot{q}_1 = 0$. Finally, substituting (20),(21) with $q_2 = 0$ and $F_y < k_t/l$ in the equation $\ddot{z} = 0$ gives the solution $\dot{q}_2 = 0$. Thus, all trajectories within the manifold $z(t) = 0$ are defined by $\dot{q}_1 = \dot{q}_2 = 0$. Consequently, $p = 0$ and $\dot{p} = 0$, which substituted in (6) give $\nabla_q V'_d = 0$ and finally $q = q^*$ from (16) hence the equilibrium q^* is locally asymptotically stable ■

Corollary 1: Consider the closed-loop system (10),(17) in the presence of physical damping $R = R^T > 0$. Then $q^* = (q_1^*, 0)$ is an asymptotically stable equilibrium if $Rml|\dot{q}|^2 \geq |\dot{F}_y|$.

Proof: Although physical damping could compromise stability in IDA-PBC, this is not the case here since $\mathcal{M}_d = k_m\mathcal{M}$ [29]. Accounting for the damping matrix $R = R^T > 0$ in (18) gives:

$$\dot{p} = -\nabla_q H - R\nabla_p H + \nabla_q W + G'u \tag{22}$$

Substituting (17) into (22) and recalculating (19) gives:

$$\dot{H}_d' = -k_v\left(\frac{z}{k_m}\right)^2 - \dot{q}^T\left(\frac{R}{k_m}\right)\dot{q} + \dot{F}_y\frac{\cos(q_2)}{mlk_m} \tag{23}$$

If $|\dot{q}|^2 Rml \geq |\dot{F}_y|$ it follows from (23) that $\dot{H}_d' \leq 0$ for any $k_v > 0$ thus $\dot{q} \in \mathcal{L}^\infty \cap \mathcal{L}^2$. According to *Assumption 2-3* also $\dot{p} = \ddot{q} \in \mathcal{L}^\infty$ and consequently $\dot{q}$ converges to zero. Therefore $p, \dot{p}$ converge to zero, and $\nabla_q V_d' = 0$ from (6), which implies that $q = q^*$ from (16) hence asymptotic stability of the equilibrium q^* is concluded. Finally, the result is global if $Rml|\dot{q}|^2 \geq |\dot{F}_y|$ for all $\dot{q}$ ■

Remark 1: Choosing the conventional quadratic solution $\Phi(w) = w^2$ in (15) is not appropriate since it would result in $\nabla_q V_d'(q_1^*, q_2^*) \neq 0$. Instead, omitting the partial feedback linearization (10), the potential-energy PDE (14) becomes:

$$\frac{\partial V_d}{\partial q_2} = \frac{1}{k_m}\left(k_t\, q_2 - F_y l \sin(q_2)\right) \tag{24}$$

In this case, $\Phi(w) = w^2$ and $w = q_1 - q_1^*$ satisfy the minimum conditions. Additionally, $u = v$ thus (17) becomes a linear control law, which represents the baseline in this work:

$$u = F_y - k_p(q_1 - q_1^*) - k_v\dot{q}_1/k_m \tag{25}$$

A nonlinear version of (25) is constructed for comparison purposes with $\Phi(w) = \log(w)^2$ and either $w = q_1^* - q_1 + 1$ or $w' = q_1 - q_1^* + 1$ which gives:

$$u = F_y + k_p \log(w)\,/w - k_v\dot{q}_1/k_m \tag{26}$$

Thus in this case the partial feedback linearization (11) provides more design flexibility and serves a similar purpose to employing a generic closed-loop inertia matrix $\mathcal{M}_d \neq k_m\mathcal{M}$. The advantage is that solving the kinetic-energy PDE (8.a) is trivial. This is particularly beneficial since analytical solutions of the kinetic-energy PDE only exist in specific cases.

Remark 2: An assessment of different actuation strategies can be conducted inspecting the two minimum conditions (16). For instance, employing a bevel-tip needle in conjunction with a rotation of the base proved effective in controlling needle deflection during insertions in soft tissue [9]. To assess the benefit of this actuation strategy within the IDA-PBC scheme, a lateral tip force $F_x = cF_y$ is introduced in the model dynamics (2), where $c = \tan(\alpha)$ and α is the angle of the bevel. The work of the external forces becomes then $W = -F_y(q_1 + l\cos(q_2)) + F_x l\sin(q_2)u'$, where a second control input $u' = -\text{sign}(q_2) = \pm 1$ is introduced to rotate the needle thus changing the plane of bending as soon a deflection occurs. Applying the feedback linearization (11) and solving the PDE (13) gives:

$$V_d'' = V_d' - \frac{u'}{mlk_m}F_x \sin(q_2) \tag{27}$$

Evaluating the minimum conditions for (27) we have:

$$\nabla_q V_d''(q_1^*, q_2^*) = \begin{bmatrix} 0 \\ -\dfrac{F_x u'}{mlk_m} \end{bmatrix} \tag{28.a}$$

$$\nabla_q^2 V_d''(q_1^*, q_2^*) = k_p\left(k_t - F_y l\right)/(mk_m^2) \tag{28.b}$$

It follows form (28) that $q^* = (q_1^*, 0)$ is a minimizer of (27) only if $F_x = 0$ and $F_y < k_t/l$ since u' can only switch between the values 1 and -1. This finding is in agreement with the literature advocating the use of bevel-tip needles for curved insertion paths rather than for straight insertions. Instead, the ability to continuously vary the lateral force F_x is required to provide full control of the deflection and achieve straight insertion paths. The latter strategy was implemented in [15] applying a controlled force near the puncture site. In practice, the main limitation of this approach is that it requires an actuator in close proximity to the puncture site, which might not be feasible in some percutaneous interventions.

IV. Simulation Results

Simulations were conducted in Matlab® with the ode23 solver. The following set of parameters representative of needle insertions in soft tissues were employed for system (2): $m = 0.001$ Kg ; $M = 0.05$ Kg ; $l = 0.18$ m ; $k_t = 0.13$ Nm . The values of k_t and l follow from (1) with $E = 120$ GPa; $I = 0.1$ mm^4; $L = 0.2$ m; $\gamma_\theta = 0.9$; $k_\theta = 2.4$, which refer to a 18G titanium needle (OD $= 1.27$ mm, ID $= 0.84$ mm). The buckling load $P_1 \cong 0.72$ N is comparable to typical insertion forces. In order to model the needle insertion forces [7], the following expression of F_y was used in the simulation, where c_0, c_1, c_2, c_3 are positive constants:

$$F_y = \left(c_0 + c_1 y_{tip} + c_2\tanh\left(c_3\dot{y}_{tip}\right)\right)\frac{k_t}{l} \tag{29}$$

The terms $y_{tip} = q_1 + (\cos(q_2) - 1)l$ and $\dot{y}_{tip} = \dot{q}_1 - \dot{q}_2\sin(q_2)\,l$ are respectively the tip position and the tip velocity. The parameter c_0 represents the fracture force of the tissue, the parameter c_1 accounts for the elastic force due to tissue deformation. The parameter c_2 represents friction forces, including Coulomb and viscous friction, and the function $\tanh(\cdot)$ is a smooth implementation of the sign$(\cdot)$ function which is used to reduce simulation runtime. Finally, the parameter c_3 is a scaling factor applied to the insertion speed. For demonstrative purposes, the numerical values of the parameters have been set to: $c_0 = 0.75$; $c_1 = 2.2$ and alternatively $c_1 = 2.5$; $c_2 = 0.25$; $c_3 = 100$. Substituting these values in (29) the force F_y varies in the interval $3/4\,P_1 < F_y < 5/4\,P_1$ which is representative of needle insertions in soft tissue, thus buckling is likely to occur in in these conditions. While in a real needle insertion the surrounding tissue would act on the needle with a lateral distributed load, this effect is minor during the initial puncture and is neglected here for simplicity. The controller (11)-(17) has been implemented with the following tuning parameters: $k_p = 10$; $k_v = 3$, $k_m = 1$. Since very large deflections were registered for the baseline controller (23) with the same values, the following parameters

have been used to provide a meaningful comparison: $k_p = 2$; $k_v = 15$. The desired insertion depth $q_1^* = 0.1$ m is reached within 30 seconds in all the simulations, which is representative of percutaneous interventions [1], [2].

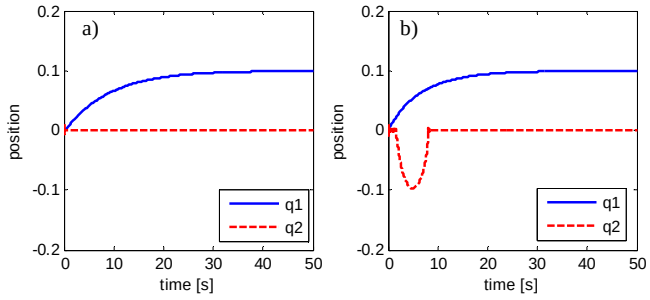

Fig. 2. Time history of the position q with $c_1 = 2.2$: a) control (11)-(17); b) control (25). The prescribed insertion depth is $q_1^* = 0.1$m.

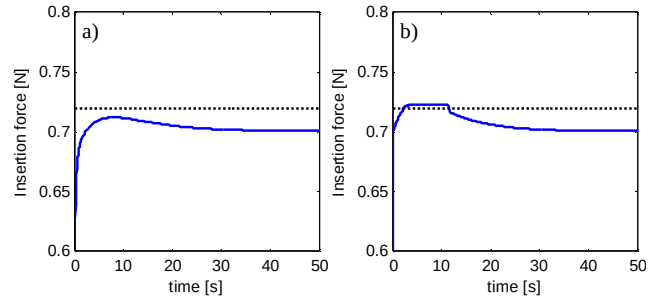

Fig. 3. Insertion force with $c_1 = 2.2$: a) control (11)-(17); b) control (25).

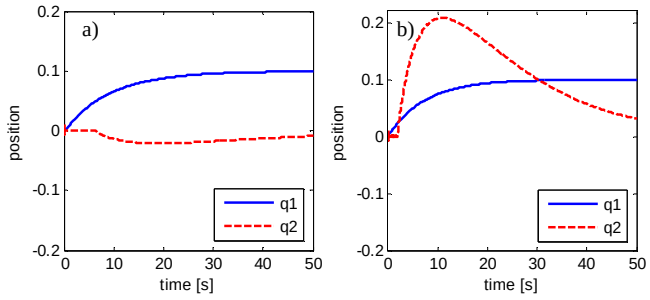

Fig. 4. Position q with $c_1 = 2.5$: a) control (11)-(17); b) control (25).

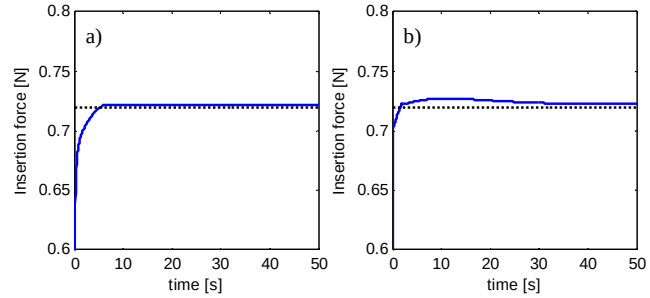

Fig. 5. Insertion force with $c_1 = 2.5$: a) control (11)-(17); b) control (25).

The time history of the position q with $c_1 = 2.2$ is shown in Figure 2. While the lateral deflection remains close to zero with control (11)-(17), it increases rapidly with control (25). Similarly, the actuation force increases more gradually with control (11)-(17), as highlighted in Figure 3 and remains below the buckling load. The time histories of the position q and the insertion force with $c_1 = 2.5$, which corresponds to a stiffer tissue, are depicted in Figure 4 and Figure 5. In this case, a non-zero deflection is observed with both controllers since the insertion force reaches the buckling load P_1. Nevertheless, the deflection is considerably smaller with controller (11)-(17). Finally, the nonlinear control (26) with $w = q_1^* - q_1 + 1$ reduces the lateral deflections compared to the linear baseline (25). However, it is less effective than the proposed control (11)-(17) as shown comparing Figure 6 and Figure 4. Similar results are obtained introducing small lateral forces (e.g. $F_x = 0.2$ N).

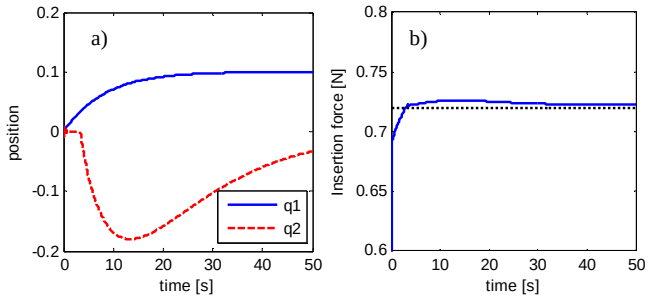

Fig. 6. Nonlinear control (26): a) time history of the position q for $c_1 = 2.5$; b) corresponding insertion force.

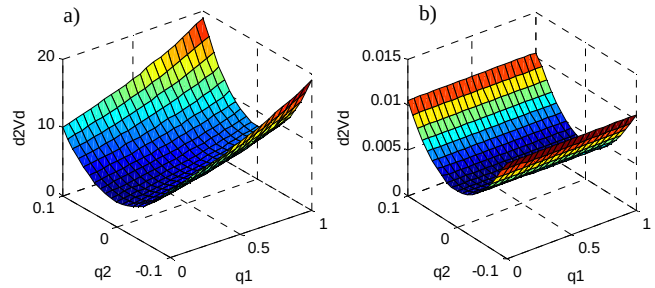

Fig. 7. Numerical values of $\nabla_q^2 V_d'$ for control (11)-(17); b) values of $\nabla_q^2 V_d$ for control (25).

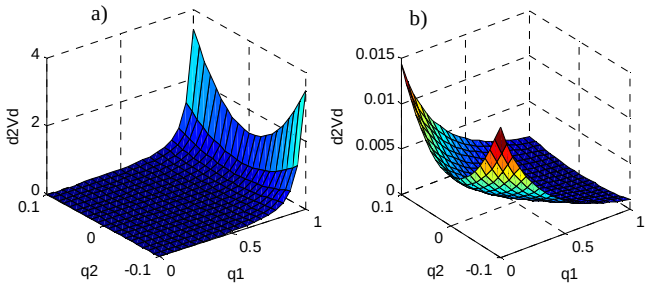

Fig. 8. Numerical values of $\nabla_q^2 V_d$ for control (26): a) $w = q_1^* - q_1 + 1$; b) $w' = q_1 - q_1^* + 1$.

Comparing the closed-loop potential energies provides further insight on the differences between controller (11)-(17), control (25), and control (26). To this end, the values of $\nabla_q^2 V_d'$and $\nabla_q^2 V_d$ for different positions q around the equilibrium q^* are plotted in Figure 7. Firstly, the magnitude of the plots is different even if the same parameters are employed (i.e.

$k_p = 10, k_m = 1$). This effect is due to the partial feedback linearization (11) that scales $\nabla_q^2 V_d'$ by a factor $1/m$. Additionally, while $\nabla_q^2 V_d'$ increases with q_1, $\nabla_q^2 V_d$ does not depend on q_1, therefore the insertion force is modulated more gradually with the controller (17). Control (26) with $w = q_1^* - q_1 + 1$ shows that $\nabla_q^2 V_d$ increases with q_1 and consequently the actuation force is smaller during the initial phase of the insertion. Although this trend is similar to $\nabla_q^2 V_d'$ (see Figure 7.a), $\nabla_q^2 V_d$ shows a steeper variation with q_1 (see Figure 8.a) which explains the better performance of control (11)-(17). Instead, employing $w' = q_1 - q_1^* + 1$ in (26) the insertion force decreases with q_1 (see Figure 8.b) thus resulting in even larger deflections. Since the performance of the controllers depends on the tuning parameters k_p, k_v, k_m, lateral deflection can be further reduced decreasing k_p and k_m, and increasing k_v. However, this could result in a slower needle insertion, which might conflict with the requirements of the clinical procedure (e.g. needle insertions under breath-hold should typically be completed within a few seconds).

V. Conclusions

The control problem for a cantilever beam with tip load and base actuation was investigated. An energy shaping controller that accounts for external forces was designed employing a rigid-link model and stability conditions were discussed. The effectiveness of the proposed controller compared to a linear baseline and to a nonlinear alternative was demonstrated with numerical simulations employing a representative model of the insertion forces. In our future work we intend to validate the results experimentally with needle insertions in phantoms. Further objectives include the study of different actuation strategies and of different models of the needle.

Acknowledgment

This research was supported by the Engineering and Physical Sciences Research Council (grant number EP/R009708/1). The Authors are grateful to Prof Ferdinando Rodriguez y Baena and to Prof Alessandro Astolfi for helpful suggestions on simulations and stability analysis.

References

1 Moche M, Heinig S, Garnov N, Fuchs J, Petersen T-O, Seider D, Brandmaier P, Kahn T, et al., "Navigated MRI-guided liver biopsies in a closed-bore scanner: experience in 52 patients," Eur. Radiol., vol. 26, no. 8, pp. 2462–2470, 2015.

2 Franco E, Ristic M, Rea M, and Gedroyc W M W, "Robot-assistant for MRI-guided liver ablation: A pilot study," Med. Phys., vol. 43, no. 10, pp. 5347–5356, 2016.

3 Lehmann T, Rossa C, Usmani N, Sloboda R S, and Tavakoli M, "A Real-Time Estimator for Needle Deflection During Insertion Into Soft Tissue Based on Adaptive Modeling of Needle–Tissue Interactions," IEEE/ASME Trans. Mechatronics, vol. 21, no. 6, pp. 2601–2612, 2016.

4 Okamura A M, Simone C, and O'Leary M D, "Force modeling for needle insertion into soft tissue.," IEEE Trans. Biomed. Eng., vol. 51, no. 10, pp. 1707–16, 2004.

5 Fallahi B, Rossa C, Sloboda R S, Usmani N, and Tavakoli M, "Sliding-based image-guided 3D needle steering in soft tissue," Control Eng. Pract., vol. 63, pp. 34–43, 2017.

6 Franco E, Rea M, Gedroyc W, and Ristic M, "Control of a Master-Slave Pneumatic System for Teleoperated Needle Insertion in MRI," IEEE/ASME Trans. Mechatronics, vol. 21, no. 5, pp. 2595–2600, 2016.

7 Van Gerwen D J, Dankelman J, and van den Dobbelsteen J J, "Needle-tissue interaction forces--a survey of experimental data.," Med. Eng. Phys., vol. 34, no. 6, pp. 665–80, 2012.

8 Van de Berg N J, van Gerwen D J, Dankelman J, and van den Dobbelsteen J J, "Design Choices in Needle Steering—A Review," IEEE/ASME Trans. Mechatronics, vol. 20, no. 5, pp. 2172–2183, 2015.

9 Abolhassani N, Patel R V., and Ayazi F, "Minimization of needle deflection in robot-assisted percutaneous therapy," Int. J. Med. Robot. Comput. Assist. Surg., vol. 3, no. 2, pp. 140–148, 2007.

10 Watts T, Secoli R, and Baena F R y, "A Mechanics-Based Model for 3-D Steering of Programmable Bevel-Tip Needles," IEEE Trans. Robot., vol. 35, no. 2, pp. 1–16, 2018.

11 Ryu S C, Quek Z F, Koh J-S, Renaud P, Black R J, Moslehi B, Daniel B L, Cho K-J, et al., "Design of an Optically Controlled MR-Compatible Active Needle," IEEE Trans. Robot., vol. 31, no. 1, pp. 1–11, 2015.

12 Sakes A, Dodou D, and Breedveld P, "Buckling prevention strategies in nature as inspiration for improving percutaneous instruments: a review," Bioinspir. Biomim., vol. 11, no. 2, p. 021001, 2016.

13 Yang C, Xie Y, Liu S, and Sun D, "Force Modeling, Identification, and Feedback Control of Robot-Assisted Needle Insertion: A Survey of the Literature," Sensors, vol. 18, no. 2, p. 561, 2018.

14 Hauser K, Alterovitz R, Chentanez N, Okamura A, and Goldberg K, "Feedback control for steering needles through 3D deformable tissue using helical paths," in *Robotics: Science and Systems V*, 2009.

15 Lehmann T, Sloboda R, Usmani N, and Tavakoli M, "Human–Machine Collaboration Modalities for Semi-Automated Needle Insertion Into Soft Tissue," IEEE Robot. Autom. Lett., vol. 3, no. 1, pp. 477–483, 2018.

16 Tsumura R, Kim J S, Iwata H, and Iordachita I, "Preoperative Needle Insertion Path Planning for Minimizing Deflection in Multilayered Tissues," IEEE Robot. Autom. Lett., vol. 3, no. 3, pp. 2129–2136, 2018.

17 Schaeffner M, Götz B, and Platz R, "Active buckling control of a beam-column with circular cross-section using piezo-elastic supports and integral LQR control," Smart Mater. Struct., vol. 25, no. 6, p. 065008, 2016.

18 Trivedi M V., Banavar R N, and Kotyczka P, "Hamiltonian modelling and buckling analysis of a nonlinear flexible beam with actuation at the bottom," Math. Comput. Model. Dyn. Syst., vol. 22, no. 5, pp. 475–492, 2016.

19 Gandhi P S, Borja P, and Ortega R, "Energy shaping control of an inverted flexible pendulum fixed to a cart," Control Eng. Pract., vol. 56, pp. 27–36, 2016.

20 Franco E, Astolfi A, and Rodriguez y Baena F, "Robust balancing control of flexible inverted-pendulum systems," Mech. Mach. Theory, vol. 130, pp. 539–551, 2018.

21 Macchelli A and Melchiorri C, "Control by Interconnection and Energy Shaping of the Timoshenko Beam," Math. Comput. Model. Dyn. Syst., vol. 10, no. 3–4, pp. 231–251, 2004.

22 Ortega R, Spong M W, Gomez-Estern F, and Blankenstein G, "Stabilization of a class of underactuated mechanical systems via interconnection and damping assignment," IEEE Trans. Automat. Contr., vol. 47, no. 8, pp. 1218–1233, 2002.

23 Franco E, "Adaptive IDA-PBC for underactuated mechanical systems with constant disturbances," Int. J. Adapt. Control Signal Process., vol. 33, no. 1, pp. 1–15, 2019.

24 Franco E, "IDA-PBC with Adaptive Friction Compensation for Underactuated Mechanical Systems," Int. J. Control, pp. 1–29, 2019.

25 Aoki T, Yamashita Y, and Tsubakino D, "Vibration suppression for mass-spring-damper systems with a tuned mass damper using interconnection and damping assignment passivity-based control," Int. J. Robust Nonlinear Control, vol. 26, no. 2, pp. 235–251, 2016.

26 Yu Y-Q, Howell L L, Lusk C, Yue Y, and He M-G, "Dynamic Modeling of Compliant Mechanisms Based on the Pseudo-Rigid-Body Model," J. Mech. Des., vol. 127, no. 4, p. 760, 2005.

27 Howell L L, Midha A, and Norton T W, "Evaluation of Equivalent Spring Stiffness for Use in a Pseudo-Rigid-Body Model of Large-Deflection Compliant Mechanisms," J. Mech. Des., vol. 118, no. 1, p. 126, 1996.

28 Mattioni A, Wu Y, Ramirez H, Gorrec Y Le, and Macchelli A, "Modelling and control of a class of lumped beam with distributed control," IFAC-PapersOnLine, vol. 51, no. 3, pp. 217–222, 2018.

29 Gómez-Estern F and Van der Schaft A J, "Physical Damping in IDA-PBC Controlled Underactuated Mechanical Systems," Eur. J. Control, vol. 10, no. 5, pp. 451–468, 2004.